BC RESEARCH ARTICLE



A farnesoid X receptor T296I variant disrupts ligand-induced FXR activation and thus bile acid transport in progressive familial intrahepatic cholestasis

Received for publication, April 28, 2025, and in revised form, September 15, 2025 Published, Papers in Press, September 29, 2025 https://doi.org/10.1016/j.jbc.2025.110769

Annika Behrendt¹, Alex Bastianelli², Jan Stindt³, Eva-Doreen Pfister⁴, Malte Sgodda 6, Tobias Cantz 6, Annika Behrendt Sebastian Hook^{5,6}, Mohanraj Gopalswamy¹, Kathrin Grau¹, Stefanie Brands¹, Carola Dröge^{2,3}, Amelie Stalke⁷, Michele Bonus¹, Sabine Franke⁸, Ulrich Baumann⁶, Verena Keitel^{2,3,*}, and Holger Gohlke^{1,9,*}

From the ¹Institute for Pharmaceutical and Medicinal Chemistry, Heinrich Heine University, Düsseldorf, Germany; ²Medical Faculty, Department of Gastroenterology, Hepatology and Infectious Diseases, University Hospital Magdeburg, Otto von Guericke University, Magdeburg, Germany; ³Medical Faculty, Department of Gastroenterology, Hepatology and Infectious Diseases, University Hospital Düsseldorf, Heinrich Heine University, Düsseldorf, Germany; ⁴Pediatric Gastroenterology and Hepatology, Department for Pediatric Kidney, Liver and Metabolic Diseases, Hannover Medical School, Hannover, Germany; ⁵Department of Gastroenterology, Hepatology, Infectious Diseases and Endocrinology, Hannover Medical School, Hannover, Germany; ⁶Research Center for Translational Regenerative Medicine, Hannover Medical School, Hannover, Germany; ⁷Department of Human Genetics, Hannover Medical School, Hannover, Germany; ⁸Institute of Pathology, University Hospital Magdeburg, Otto von Guericke University, Magdeburg, Germany; ⁹Institute of Bio- and Geosciences (IBG-4: Bioinformatics), Forschungszentrum Jülich GmbH, Jülich, Germany

Reviewed by members of the JBC Editorial Board. Edited by Qi-Qun Tang

Nuclear receptor farnesoid X receptor (FXR) acts as a key regulator of bile acid pool homeostasis and metabolism. Within the enterohepatic circulation, reabsorbed bile acids act as FXR agonists. FXR, in turn, transcriptionally controls the synthesis and transport of bile acids. Binding occurs in the ligand binding domain (LBD), favoring a conformational change to the active state in which helix 12 interacts with the LBD to form an interaction surface for nuclear co-activators. The homozygous missense variant T296I, identified in a patient with progressive familial intrahepatic cholestasis (PFIC), is located close to the critical helix 12 interaction. Here, we identified reduced transcriptional activity of the variant protein on the downstream targets bile salt export pump (BSEP) and small heterodimer partner (SHP) in vitro, within the patient's liver, and in iPSC-derived hepatic organoids. BSEPdependent Tauro-DBD transport was impaired in T296I patient-derived organoids, but could be rescued via lipid nanoparticle-mediated FXR WT mRNA delivery, indicating the variant is responsible for the identified reduced BSEP expression. Using molecular dynamics simulations, we observed a reduced transition from the inactive to the active state for the T296I variant, indicating a molecular mechanism underlying the reduced activity. To our knowledge, this is the first study to describe the conformational change from an inactive to an active state of the FXR LBD. This might be useful for new therapeutic approaches targeting the activation of FXR.

Farnesoid X receptor (FXR), encoded by the NR1H4 gene, is a nuclear receptor (NR) responsive to bile acids (BA) and a key regulator of BA metabolism, playing a pivotal role in maintaining BA homeostasis by controlling BA synthesis, transport, and detoxification (3, 4). Amongst other targets, the ABCB11 gene (encoding for the bile salt export pump (BSEP)) and the NROB2 gene (encoding for the small heterodimer partner (SHP)) are transcriptionally regulated by FXR (3, 4). NR1H4 variants associated with PFIC (FXR-deficiency, also named PFIC subtype 5) were characterized by a secondary BSEP deficiency, coagulopathy and a rapid progression toward end-stage liver disease (5-8). While most patients carried bi-allelic protein-truncating variants (5-7, 9), only two NR1H4-associated PFIC patients carrying homozygous missense variants have been described to date (7, 10). One patient died on the transplant waiting list due to end-stage liver disease at the age of 9 months (c.557 G > A) (7), while the other patient was successfully transplanted at the age of 8 months (c.887 C > T, p.(Thr296Ile), referred to as T296I in the following) and is currently 10 years old (10). For further information on the patient and clinical data, please refer to the initial report (case 4) (10). Staining of FXR and the bile salt export pump (BSEP) was found negative in the liver tissue of PFIC patients with protein-truncating NR1H4 variants (5, 9). To determine the contribution of the homozygous NR1H4 T296I missense variant to the PFIC phenotype of our patient, we studied the localization and transcriptional activity of the

^{*} For correspondence: Holger Gohlke, gohlke@uni-duesseldorf.de; Verena Keitel, verena.keitel-anselmino@med.ovgu.de.



Progressive familial intrahepatic cholestasis (PFIC) is a rare group of genetic disorders that affect the liver's ability to excrete bile constituents, resulting in impaired bile flow, subsequent intrahepatic cholestasis, and progressive liver damage and failure (1, 2).

mutated protein in vitro. We further used the known intrahepatic cholestasis of pregnancy (ICP)-associated M173T FXR variant (11) to compare variant effects (Figs. S2 and S3). To unravel the impact of the T296I variant on the structural dynamics of the protein at an atomic level, we further used molecular dynamics (MD) simulations. MD simulations have proven useful in elucidating the functional mechanisms of protein activity (12). In particular, nuclear receptors (NRs) have benefited from this in-depth analysis as their functions are often diverse, and subtle changes in ligands can lead to altered conformations and, thus, protein activity (13-15). The positioning of helix 12 (H12), forming part of the activation function 2 (AF2) surface, is pivotal for NR activity via the recruitment of coregulatory proteins. Coactivators interact with the AF2 surface using a conserved LXXLL motif (16), while antagonist-bound NRs favor corepressor binding to the AF2 surface with a larger hydrophobic motif and blocking the active positioning of H12 (17). Several MD studies of the LBD of FXR have underlined the importance of H12 positioning (18-20). However, the transition from the inactive to the active conformation as well as the effect of single-site missense variants on the function of FXR has so far not been analyzed by MD studies. Thus, we employed MD simulations to analyze the conformational change from an inactive to the active state and evaluated the impact of the T296I variant both with a localized distance measurement and with regard to its influence on H12 positioning. To our knowledge, this is the first simulation study to explicitly investigate the

transition between the inactive and the active state of the FXR LBD, uncovering the conformational change of H12.

Results

The T296I variant is located within the LBD of FXR

The ligand-binding domain (LBD) of FXR is critical in regulating the protein's activity. Residue 296 is located on helix 3 with its side chain facing toward the AF2 interaction surface formed partly by H12 (Fig. 1, A and B). We thus hypothesized that variant T296I impacts FXR's ability to transition from the inactive to the active state. Accordingly, we investigated the effect of variant T296I in MD simulations starting from one of the four configurations: FXR WT in the active state ("active WT"), FXR T296I variant in the active state ("active T296I"), FXR WT in the inactive state ("inactive WT"), and FXR T296I variant in the inactive state ("inactive T296I") (Fig. 1C). All systems contained the LBD of FXR, the agonist chenodeoxycholic acid (CDCA) (21, 22), and a short peptide sequence of the nuclear receptor coactivator 2 (NCoA2). This setup was chosen to drive the inactive state toward the active state, since the presence of agonists and coactivators has been shown to stabilize the active state (15). The inactive state was created from the active state through repositioning of the loop region between helix 11 and H12 such that H12 pointed away from the LBD core and had a distance > 45 Å to it (distance in the active state 16 Å). The setup allowed us to study if the substitution impacts the active

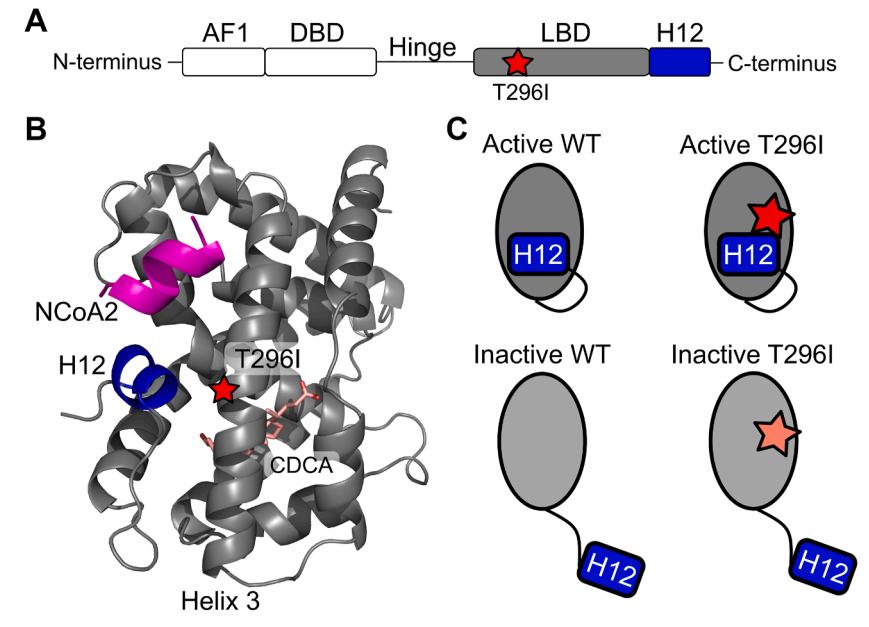


Figure 1. Overview of the protein structure of FXR and the variant site within the LBD. A, schematic of the domain arrangement of the FXR protein. The N-terminal activation function 1 (AF1) motif is followed by the DNA-binding domain (DBD), which is connected *via* a flexible hinge region to the LBD and the C-terminal H12. The variant T296I (*red star*) is located within the LBD. B, protein structure of the LBD of FXR. The protein systems were modeled based on the crystal structure of agonist-bound FXR LBD (15) and used for MD simulations, containing additionally CDCA as ligand (*pink*, shown as *sticks*) and a short peptide of NCoA2 (*magenta*). H12 is highlighted in *blue* and helix 3, containing the variant site T296I (*red star*), is labeled. The close distance of position 296 to H12 in the active position suggests a potential impact on the conformational change from the inactive to active state. C, overview of the four systems used as input to MD simulations to study the variant's impact on the active and inactive state of the LBD. To differentiate between the different systems, we have consistently used the following color scheme: active WT in *darker grey*, inactive WT in *lighter grey* (corresponding to the depicted color of the LBD), active T296I in *red* and inactive T296I in *faded red* (corresponding to the depicted color of the star indicating the variant position).

state and/or the transition from the inactive to the active state. The ICP-associated M173T variant is located in the DNA-binding domain of FXR and, accordingly, cannot be analyzed with this MD simulations setup.

T296I decreases the transcriptional activity of FXR

To determine the consequences of the FXR missense variant T296I on expression, subcellular localization and target gene induction, human FXRa1 and FXRa2 were cloned from human liver and co-transfected with RXRa into HEK293 cells. Both wildtype (WT) and the missense variant were detected within the nucleus of transfected cells (Fig. 2A). Furthermore, protein amounts as determined by western blotting were similar in WT and T296I transfected cells (Fig. 2B). For functional analysis, we used a luciferase expression vector containing the BSEP promoter sequence (BSEP^{prom}-Luc.), which was co-transfected with combinations of RXRa and either FXRa1WT, FXRa2WT, FXRa1T296I, or FXRα2^{T296I}. The variant effect was further analyzed in transfections without the heterodimer partner RXRα (Fig. S1). The cells were stimulated with an RXR ligand (9-cis-RA, 1 μM) and the endogenous FXR agonist CDCA at different concentrations (Fig. 2, C and D; Fig. S2, A and B). We further validated if the absence of the sodium taurocholate cotransporting polypeptide (NTCP) impacts assay results by additionally co-transfecting cells with NTCP (Fig. S2A). Our results indicate that the presence of NTCP does not alter the overall variant impact, in line with evidence that passive diffusion is the main factor for CDCA uptake into hepatocytes (23).

Luciferase activity showed an increase in response to transfection with FXRa1/2 and, additionally, a dosedependent transactivation of BSEP in response to CDCA (24). The highest BSEP transactivation was observed when both RXR and WT FXRα1/2 were co-transfected, respectively and cells were stimulated additionally with 9-cis-RA and CDCA 25 µM, which was accordingly represented as 100% luciferase activity (Fig. 2, C and D). This is in line with previous data showing that the BSEP promoter is regulated by the FXR/RXR heterodimer (25). The T296I variant resulted in a reduced transcriptional activity in both FXR isoforms (Fig. 2, C and D), independent of the used CDCA concentration (0, 1, 10, or 25 µM). T296I showed a significant decrease of basal BSEP transactivation with 22.5% and 14.7% for the FXRα1 and FXRα2 isoforms, respectively, compared to 41.1% and 39.7% for the FXR WT α 1/ α 2 isoforms in the absence of CDCA. Basal activity for both FXR isoforms has been identified previously (24, 26). At 1 µM CDCA treatment, the T296I variant reached 22.1% and 13.1% of luciferase activity, while the wildtype FXRα1 and FXRα2 isoforms showed significantly higher luciferase activity at 48.4% and 63.6%, respectively. At a dose of 10 µM CDCA the variant reached 24.9% and 14.3% of luciferase activity, while the FXR WT isoforms showed responses with 80.4% and 96.4%, respectively. At 25 µM CDCA, the variant showed significantly reduced luciferase activity of 31.6% and 16.0%, compared to the maximal response of FXR WT α 1/ α 2, set to 100% for each isoform. The activity of the T296I variant increased with higher ligand concentration (Fig. S2C), supporting the hypothesis that the variant did not impair ligand binding as indicated by non-significant changes in the melting points of

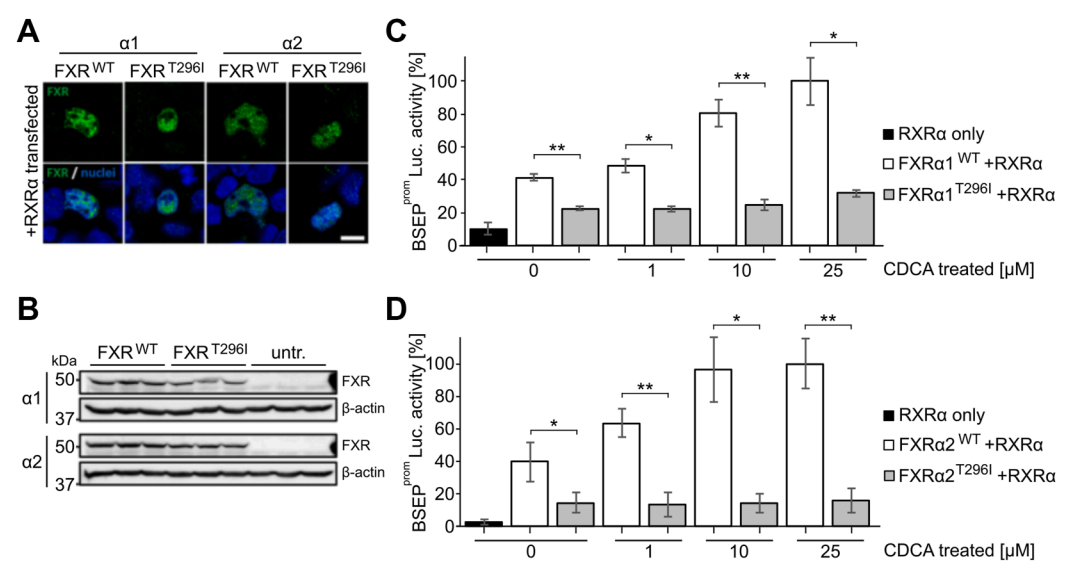


Figure 2. FXR T296I reduces transcriptional activity of the BSEP promoter in transfected HEK293 cells. *A*, HEK293 transiently co-transfected with RXRα and either FXRα1^{WT}, FXRα2^{WT}, FXRα1^{T296I}, or FXRα2^{T296I} showed correct nuclear localization of the wildtype (WT) and mutant protein. Bar: 10 μm. B, Western blot analysis revealed similar protein amounts in cells transfected with the different FXR cDNA constructs, untr.: untransfected controls. See Fig. S13 for uncropped Western blots. C, analysis of luciferase enzymatic activity after transfection of HEK293 cells with a luciferase reporter gene downstream of the BSEP promoter (BSEP^{prom}-Luc) as well as different combinations of RXRα and either FXRα1^{WT} or FXRα1^{T296I}, as indicated on the x-axis. Cells were stimulated with the FXR ligand CDCA at indicated concentrations and the RXR ligand 9-cis-RA (1 μM). Values were obtained from three independent experiments, in which each condition was tested in triplicates. Values on the y-axis represent the mean and SD, expressed as % luciferase activity. The asterisks indicate a significant difference analyzed by a two-tailed Student's t test. D, analysis of luciferase enzymatic activity after transfection of HEK293 cells with RXR α and either FXR α 2 WT or FXR α 2 1296 , as indicated on the x-axis. Further conditions were the same as for the FXR α 1 isoform in



FXR WT or variant – obeticholic acid (OCA) complexes (Figs. S7–S9) or determination of the apparent K_D of OCA or CDCA against FXR LBD WT or FXR LBD variant, respectively, from monitoring changes in the intrinsic tryptophan fluorescence intensity of the protein upon incubation with different ligand concentrations (Figs. S7 and S10). Furthermore, the T296I variant reduced transcriptional activity of the SHP promoter, another FXR target (Figs. S1B and S2D).

In summary, although the subcellular localization and protein expression levels were unaffected, the presence of the T296I missense variant resulted in a significant decrease in the transactivation of FXR target genes in vitro.

FXR T296I leads to an increased distance between H12 and the substitution site, indicative of a less favorable active state

Using MD, we investigated the molecular mechanisms underlying the decreased activity of the T296I variant. All simulation systems showed minor structural variability with respect to the binding of CDCA and NCoA2 and the FXR LBD structure up to and including helix 11 (Fig. S3).

Based on the crystal structure of the FXR LBD (15), representing the agonist-bound active state, the WT T296 likely interacts with T466 preceding H12 (Fig. 3A). Accordingly, we measured the distance between residue T296 and T466 during MD simulations and compared it to the reference distance in the crystal structure. For the active states, the variant showed an increase in the distance (Fig. 3B). We determined the frequency of occurrence when the reference cutoff distance was reached (Fig. 3C, Table S1). Across the 15 replicas,

the active WT system was found in approximately 27% of the time in the active state according to distances below the reference distance. The frequency of occurrence was significantly lower for active T296I (0.40%). The inactive systems showed initially high distance values, as expected. Inactive WT reached below the reference distance in six out of 15 replicas and often stayed within this active state for the remainder of the simulation time, indicating that the active state is the preferred one under the simulation conditions (Fig. S4, Table S1). Inactive T296I only reached the reference distance in one replica (Fig. S4, Table S1) and, accordingly, the frequency of reaching the reference value was significantly reduced in the inactive T296I system compared to the inactive WT system (Fig. 3C).

Overall, we observed an increase in the distance between residue T296 and T466 for the T296I variant in the active state. In line, for systems started either from the active or inactive state, T296I led to a significant decrease in the frequency of occurrence in reaching the reference distance compared to the WT. These data indicate that the active state is destabilized in the variant.

The correct positioning of H12 in the active state is reduced in the T296I variant

As the correct positioning of H12 within NRs is crucial for activity (27-30), we visually analyzed the simulation trajectories of the inactive systems and exemplarily show the conformational change from the inactive to the active state for one out of several MD replicas of the inactive WT system

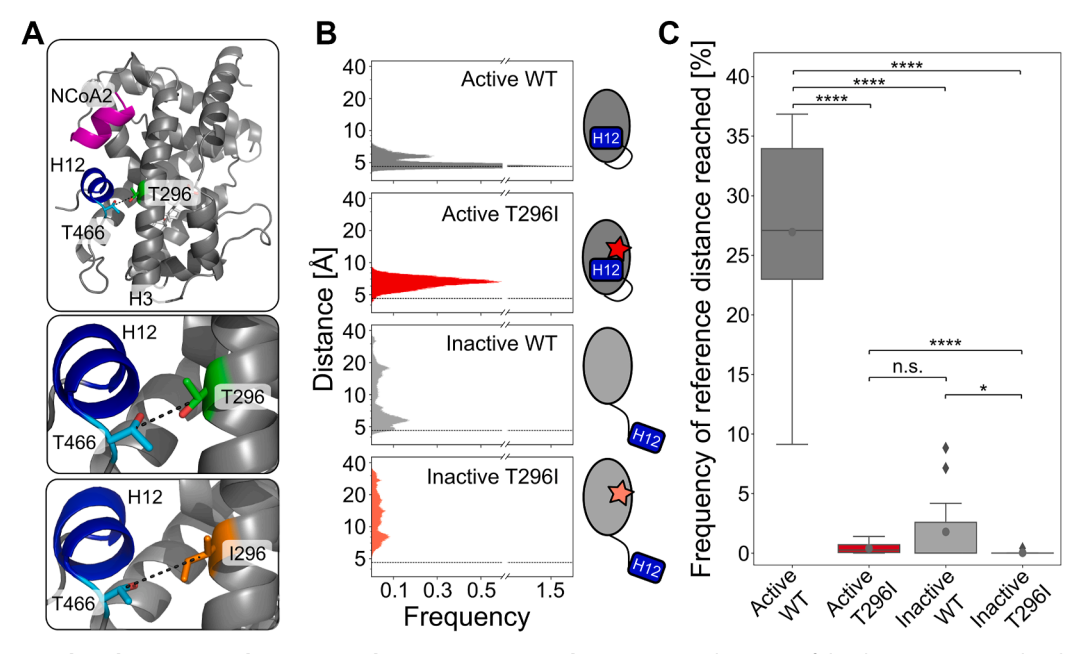


Figure 3. Distance analysis between residues T296 and T466 over MD simulation time. A, depiction of the distance measured within the LBD of FXR between the CB atoms of residue T296 and T466. The mean distance is increased in the active T296I (6.6 Å) compared to the active WT (5.0 Å). B, histograms of measured distances over all 15 MD runs (see Fig. S4) for each analyzed state. The reference distance (4.6 Å) as measured in the agonist-bound crystal structure (15) is depicted as dashed lines. C, frequency of occurrence that the respective system is in the active state. For each replica (Fig. S4), the percentage of reaching a distance below the reference distance (4.6 Å) is depicted as a boxplot. Individual values are shown in Table S1. Boxes depict the guartiles of the data with the median (straight black lines) and mean (grey dots) indicated; the whiskers indicate the minimum and the maximal values, outlier points are depicted as rhombus. Differences in the mean values were statistically evaluated using a two-sided Mann-Whitney U test (N = 15, n.s.: not significant; *: $p \le 0.05$, ****: $p \le 0.0001$).

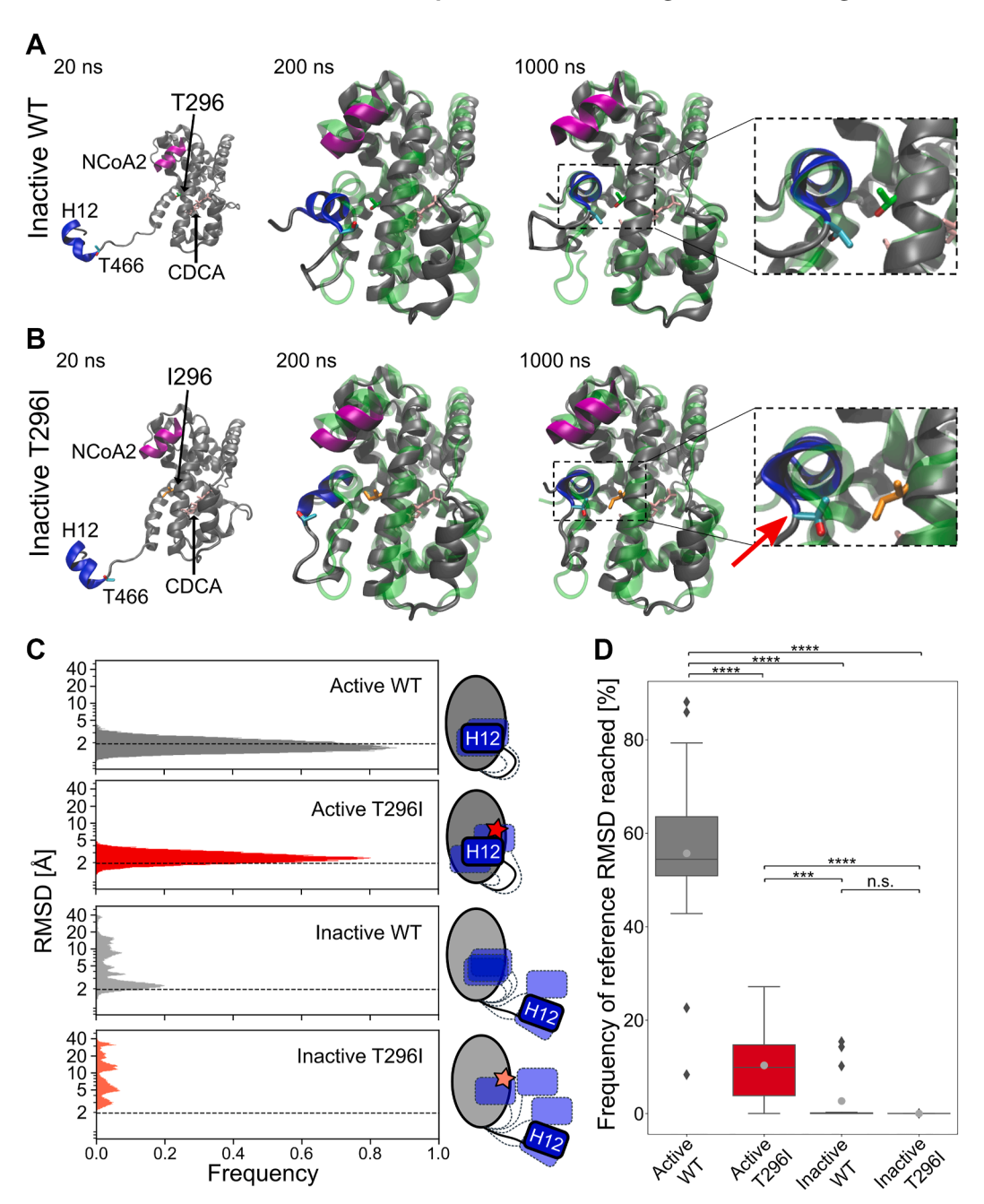


Figure 4. Positioning of H12 during MD simulations. A, conformational transitioning of the inactive WT (replica no. 2, Movie S1, Figs. S4 and S6) over the MD simulation time. The initial active state (based on the crystal structure of agonist-bound FXR LBD (15)) is depicted as a green, translucent cartoon structure. B, transitioning of the inactive T296I (replica no. 6, Movie S2, Figs. S3 and S5) over the MD simulation time. The initial active state is depicted as a green, translucent cartoon structure. Important residues (variant site 296 [green or orange, shown as sticks], T466 [cyan, shown as sticks], H12 [blue], NCoA2 [magenta], and bound ligand CDCA [pink, shown as sticks]) are additionally depicted in A and B. After 1000 ns, H12 of the inactive WT showed good alignment with the active structure, while H12 of the inactive T296I showed structural deviations (red arrow). C, histograms of RMSD values of H12 and the preceding T466 over all 15 MD replicas for each analyzed state. Data for each MD replica are depicted in Fig. S5. A skewed Gaussian function was fitted to the distribution of active WT (Fig. S5), and the obtained mean (1.9 Å) was used as a reference cutoff (dashed lines). D, frequency of occurrence of a system spends in the active state, i.e., when the reference cutoff is reached. For each replica (Fig. S6), the frequency of occurrence was determined and depicted within boxplots. Individual values are shown in Table S2. Boxes depict the quartiles of the data with the median (straight black lines) and mean (grey dots) indicated; the whiskers depict the minimum and the maximum values, and outlier points are depicted as rhombus. Differences in the mean values were statistically evaluated using a two-sided Mann-Whitney U test (N = 15, n.s.: not significant; ***: $p \le 0.001$, ****: $p \le 0.0001$).

showing this transitioning (Fig. 4A and Movie S1). For the inactive T296I, we show the MD replica where H12 positioning was closest to the conformation in the active state (Fig. 4B and Movie S2). Further, we analyzed the impact of T296I on the positioning of H12 using the root mean square

deviation (RMSD) of residues 466 to 473 (H12 and preceding T466) over the MD simulation time (Fig. 4, C and D). As a reference state, we employed the active conformation based on the crystal structure of the agonist-bound FXR LBD (15). For the active WT, a skewed Gaussian function was fitted to



the RMSD histogram, yielding a mean of 1.9 Å (Figs. S5 and 4C). Over the entire MD simulations, more than half of the time (\sim 56%, Table S2 and Fig. 4D), the active WT had an RMSD below this mean value, which we used as a further reference to indicate reaching the active state. Comparing the active systems revealed a significant shift in the distributions, with a larger mean of active T296I indicating a higher deviation from the active positioning (active WT mean: 1.9 Å, active T296I mean: 2.6 Å, p = 0.0022, two-sided t test, Fig. S5). The frequency of reaching the active state was significantly lower for active T296I, inactive WT, and inactive T296I systems compared to active WT (Fig. 4D). While the inactive WT reached the reference RMSD value in four out of 15 replicas, the inactive T296I reached it in one replica (Fig. S6). Furthermore, while the inactive T296I did not stay in the active state long (frequency: 0.01% in replica no. 6), the inactive WT -once reaching the active state-showed often prolonged persistence times (frequency: 15.40% in replica no. 2, 0.26% in replica no. 6, 10.17% in replica no. 8, 14.29% in replica no. 13) (Fig. S6 and Table S2). The comparison between inactive WT and inactive T296I indicated a similar trend as observed for the distance analysis but did not reach the significance level (Fig. 4D). Of note, the variant showed no marked structural impairment in other regions, such as the stability of helix 3. The positioning of the co-activation peptide, although most flexible in the inactive state of the variant, showed no significant difference from the inactive state of the WT (Fig. S3E).

Overall, H12 positioning is significantly structurally deviating with respect to the reference active state for all systems compared to the active WT. While the active T296I could reach the reference cutoff, it did so for a significantly decreased amount of time compared to the active WT, again indicating that the active conformation is less favorable in the variant. Although inactive WT and inactive T296I could both reach the cutoff, the inactive WT reached it more frequently and for a longer time. However, the differences to inactive T296I are not significant. Our data indicate that unbiased MD simulations on the µs-scale can sample the transition from the inactive to the active state (see Table 1) and that this conformational change is less frequent in the variant.

The T296I variant is associated with reduced expression of FXR target genes

To investigate the mRNA expression of FXR and two of its targets (*ABCB11* encoding BSEP and *NR0B2* encoding SHP; we have used the protein names in the following for coherence throughout the manuscript) in the PFIC patient carrying

the T296I variant, we performed qPCR analysis using FFPE samples from the patient's liver taken at the time of transplantation. Additionally, FFPE-liver samples from four cirrhotic adult patients and four healthy adult control samples were included in the analysis. To address the putatively low RNA integrity after isolation from FFPE samples, we employed TaqMan Gene Expression Assays targeting different regions of the FXR and BSEP transcripts. While FXR mRNA expression was even slightly higher for the patient than the healthy control and the cirrhosis livers (Fig. 5A), BSEP mRNA and SHP mRNA expression was strongly reduced in comparison to the healthy controls but also the cirrhotic liver samples (Fig. 5B). These findings clearly suggest that our in vitro and in silico data authentically reflect the impaired transcriptional target gene activation by the FXR T296I variant observed in the patient's liver specimen.

To get more functional insights, we reprogrammed peripheral blood mononuclear cells from the FXR T296I patient into induced pluripotent stem cells (iPSCs), which were subsequently differentiated into hepatic organoids. qRT-PCR of these patient-iPSC-derived liver organoids revealed an uncompromised expression of FXR (86.8% of healthy control), but a marked reduction of mRNA expression of FXR target genes BSEP, SHP, MDR3, and RARa (1.6, 25.8, 38.7, and 18.8%, respectively) (Fig. 5C). As the hepatic organoids build apical luminal structures resembling bile canaliculi, we were able to study the transport of the fluorescent BSEP-specific substrate Tauro-nor-THCA-24-DBD (Tauro-DBD) into such luminal cavities. After recovery of hepatic organoids from the Matrigel domes, the organoids were incubated with the fluorescent substrate for 0 min, 20 min, or 60 min at 37 °C and the proportion of fluorescence-positive luminal structures over the total area of luminal structures was assessed by fluorescence microscopy and subsequent image analysis. Control organoids exhibited intact Tauro-DBD transport capabilities (3.3% at 0 min, 25.6% at 20 min, and 75.6% at 60 min Tauro-DBD-positive area; average over seven independent measurements), while organoids obtained from the T296Imutant iPSCs did not show Tauro-DBD transport (<0.1%, <0.1% and 0.6% at the respective time points) (Fig. 5D). Lipid nanoparticle (LNP)-mediated mRNA delivery allows gene supplementation during the formation of hepatic organoids. We were able to restore BSEP-mediated Tauro-DBD transport after LNP-based delivery of BSEP-mRNA or FXRα2mRNA in the patient's iPSC-derived organoids to levels of 37.2% and 45.7%, respectively (Fig. 5E). Stimulation of FXR activity by 1 µM GW4064 resulted in an increased BSEP transport activity (65.8%), suggesting that FXR-mediated

Table 1
Overview of the MD simulation results

State/significance	Distance criteriaistance criteria	RMSD criteria
Inactive WT reaching active state	6 out of 15 runs	4 out of 15 runs
Inactive T296I reaching active state	1 out of 15 runs	1 out of 15 runs
Significance between WT and T296I ^a	$(p = 0.016)^5$	n.s. $(p = 0.076)$

^a Using one-sided t test.

 $^{^{}b} p < 0.05.$

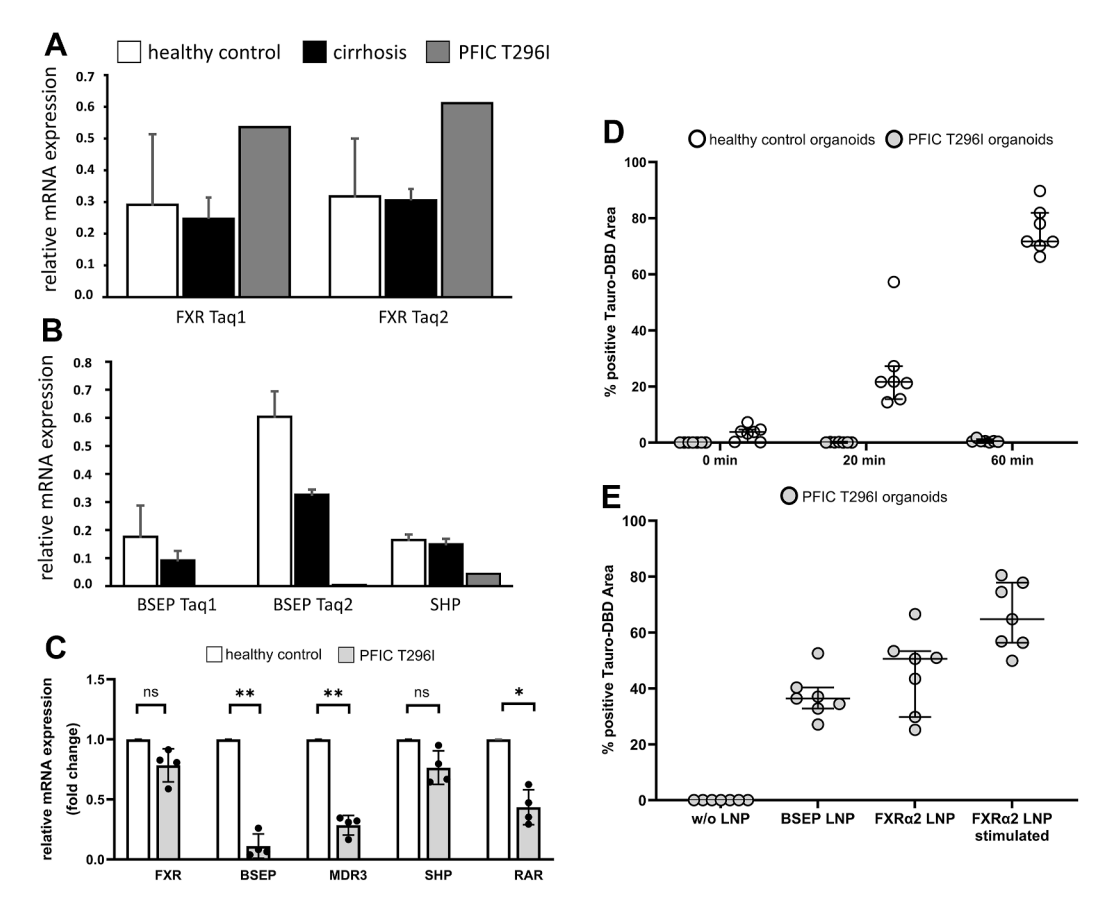


Figure 5. FXR, BSEP, and SHP expression in the patient's liver tissue and patient's iPSC-derived hepatic organoids. *A*, relative mRNA expression of FXR using two different TaqMan probes (Taq1 and Taq2) showed even higher levels in the patient's liver (*grey*) as compared to healthy controls (*white*, n = 4) or cirrhotic livers (*black*, n = 4). *B*, FXR target gene expression of BSEP and SHP were strongly reduced in the liver of the T296l PFIC patient as compared to healthy control or cirrhotic liver tissue. *C*, patient's iPSC-derived organoids exhibited FXR expression and marked reduction of target gene expression (BSEP, MDR3, RARα); results were obtained from four individual organoid differentiation experiments (mean ± SD; 1-way ANOVA analysis: *p < 0.05; **p < 0.01). *D*, functional assessment of BSEP-mediated transport of Tauro-nor-THCA-24-DBD (Tauro-DBD) exhibited proper time-dependent transport (0 min-60 min) in control iPSC-derived hepatic organoids but absence in the patient's iPSC-derived organoids (n = 7; median with interquartile range). *E*, delivery of BSEP or FXRα2 (± stimulation with GW4064) mRNA *via* lipid nanoparticles (LNP) restored Tauro-DBD transport. The % positive Tauro-DBD Area was measured after 60 min (n = 7; median with interquartile range).

signaling is authentically reflected in this iPSC-derived organoid model. This strengthens our data that the FXR T296I variant fails to activate BSEP gene expression, thus, causing a PFIC phenotype.

Discussion

In this study, we combined computational studies with *in vitro* experiments to analyze the impact of the PFIC-associated *NR1H4* T296I variant on FXR protein expression, subcellular localization, and function. While the introduction of the missense variant into the $\alpha 1$ or $\alpha 2$ FXR isoform did not affect protein expression and nuclear localization *in vitro*, it significantly reduced activation of the FXR target genes BSEP and SHP. A strong reduction of BSEP and SHP was also observed in the patient's liver at the time of transplantation and in iPSC-derived hepatic organoids of the patient, while FXR expression levels were similar or even higher than in controls. Partial rescue of the impaired BSEP-mediated Tauro-DBD transport in T296I organoids was achieved using LNP with BSEP or FXR $\alpha 2$ WT mRNA, further validating that the variant

is causative of the reduced BSEP expression and subsequent phenotype. Using our computational approach, we elucidated a detailed mechanism for the effect of the variant on the conformational transition of the LBD from the inactive to the active state. The variant showed a significantly reduced tendency to reach the active state, which can explain the *in vitro*-identified decreased target gene expression and thus the PFIC phenotype of the patient (10). Employing MD simulations for an atomistic analysis of this variant indicated a molecular mechanism underlying the protein dysfunction and showcases implications for general FXR protein activation.

We describe conformational changes from an inactive to the known active state of the FXR LBD in unbiased MD simulations. To drive the system towards the active state, we used a coactivator peptide and the most potent *in vivo* agonist CDCA (31) within the MD systems as both coactivator peptide and ligand binding have been shown to induce and stabilize the active state *in vitro* (15). Depending on the analysis, the inactive WT system reached the active state in 27% or 40% (4/15 replicas for H12 RMSD analysis and 6/15 replicas for distance analysis, respectively) of the simulations (Table 1). A

dynamic movement from the inactive to the active state (and potentially reverse, at least in ligand-free states) may occur in the nanosecond time scale as indicated by time-resolved fluorescence anisotropy decay studies on PPARγ (29). Chrisman et al. showed conformational changes of the H12 within the NR PPARy toward an almost-active state within the µs to ms time scale range in unbiased MD simulations (14). Within our MD simulations, the LBD of FXR might sample conformational spaces usually not available due to sterical hindrances either by the not considered parts of FXR (DNA binding domain and linker sequences) or due to heterodimer-binding partners. Thus, it is not surprising that in several replicas, H12 did not move into the active position within the 1µs of simulation time due to being trapped in other energy minima. Still, fast transitioning from the inactive to the active state was observable in some replicas. Comparing the difference between inactive WT and inactive T296I systems in reaching the active state, we observed a decrease by a factor of 3.8 to 5.7 (inactive WT: 26.7% or 40%; inactive T296I: 7%). This is in good agreement with the transcriptional activity reduction of T296I compared to WT, as shown in the luciferase assay for BSEP and SHP as well as the patient's liver tissue (Figs. 2 and 5). Note that we have not investigated the impact on co-regulator recruitment or other FXR functions. These limitations may be addressed through more detailed investigations, which are beyond the scope of this study but present valuable opportunities for future research.

Overall, the variant T296I, while also impacting the active state, likely exerts its negative impact on protein activity due to a change in the structural dynamics of the inactive-toactive state transition. Our results indicate that the T296I protein does not reach the active state fully and less frequently compared to the WT protein. Furthermore, from the analysis of the MD simulations, insights into the activation mechanism of the LBD were gained. The presence of the ligand and co-activation peptide allows FXR to switch into an active state and stably stay within this state. This is in line with previous NMR or MD studies in ROR γ (13), PPAR γ (14, 32), and FXR or FXR/RXR heterodimers (18-20). By contrast, the transition from inactive to active FXR has previously not been observed in MD simulations. Our setup of the MD simulations can be useful to predict the impact of other missense variants on FXR function and potentially strengthen studies on FXR targeting, enabling detailed evaluations of the molecular mechanism of drugs based on their impact on the activation transitioning.

Experimental procedures

Plasmids, cloning, and mutagenesis

The BSEP promoter plasmid based on pGL3-basic (BSEP^{prom}-Luc) was a kind gift from Roche. The human small heterodimer partner (SHP) promoter (bases -572 to +10, GenBank Accession Number AF044316) (33) was amplified by PCR from a healthy human liver genomic DNA pool. DNA sequencing was performed for all cDNAs used (Eurofins). Note that the numbering of the protein variant (T296I) is based on the alpha1 isoform (Uniprot acc. Q96RI1-1). For details on the cloning strategies and plasmids, see SI.

Immunofluorescence staining of HEK293 cells

HEK293 cells seeded onto glass coverslips in 12-well plates were transiently transfected with 1 µg each of FXR and retinoic X receptor (RXR) α expression constructs for 48h. After 24h, cells were stimulated with obeticholic acid (OCA, INT-747, 10 μM) and 9-cis-retinoic acid (9-cis-RA, 1 μM). Cells on coverslips were washed with PBS before fixation with icecold methanol (30s). After blocking in UltraVision protein block (ThermoFisher Scientific) for 30 min, cells were stained for 1h at 1:100 with rabbit anti-FXR (H-130; sc-13063, Santa Cruz Biotechnology) followed by staining at 1:250 with goat anti-rabbit-IgG-FITC (Jackson ImmunoResearch) and DAPI at 1:20.000. Coverslips were mounted on microscopic slides using Dako fluorescence mounting medium.

Western blot

HEK293 cells seeded into 6-well plates were transiently transfected for 48h with 2 µg per well of either WT or mutant pnoCherry-FXR as described above and in SI. Membranes were blocked with 5% BSA in TBS-T for 1h before overnight incubation with rabbit anti-FXR (H-130; 1:2.000) and mouse anti-β-actin (ab6276, Abcam; 1:10.000), followed by incubation with goat anti-rabbit-IgG-AlexaFluor 647 and goat antimouse-IgG-AlexaFluor 488 (both at 1:5.000). Fluorescent signals were detected using a ChemiDoc MP imaging system (Biorad).

Luciferase assay

Luciferase assays were performed using the Dual Luciferase reporter assay (Promega) according to the manufacturer's instructions. Briefly, HEK293 cells kept in DMEM containing 10% fetal calf serum (FCS) were seeded in 96-well plates at 7.000 cells per well and transfected the next morning with 100 ng of BSEP-Luc or SHP-Luc plasmid and 10 ng each of FXR and RXR expression plasmids using Fugene HD (Promega) at a 2.5:1 (reagent: DNA) ratio. Where appropriate, plasmids were replaced with equal amounts of their respective empty backbones as a control, and each well also received 5 ng of pRL-TK as an internal assay control. Cells transfected with FXRα1/2 expression plasmid were stimulated with CDCA (0, 1, 10, or 25 μM), cells transfected with RXRα were stimulated with 1 µM 9-cis-retinoic acid (9-cis-RA), and cells transfected with both FXR\alpha1/2 and RXR\alpha expression plasmids were stimulated with both ligands.

Patient iPSC-derived hepatic organoids

Induced pluripotent stem cells (iPSCs) were generated from patient peripheral blood mononuclear cells (PBMCs) with a commercial Sendai virus-based reprogramming system (Cytotune 2.0, ThermoFisher Scientific) and maintained as pluripotent stem cells on CF1 murine feeder cells according to standard conditions. Authenticity of the iPSC line was validated via patient-specific SNPs, and the absence of mycoplama contamination was confirmed. Generation of hepatic organoids was performed as described by Shinozawa et al. (34) with minor changes. In brief, cells were seeded as single cells on GelTrex-coated dishes (TPP) in E8 media containing no FGF2 but 10 µM RHO-Kinase Inhibitor (Tocris) with a density of 120.000 cells/cm². After 24 h, cells were washed and differentiated towards definitive endoderm and subsequently embedded into Matrigel (Corning) domes as described to form iPSC-derived hepatic organoids. After 9 to 11 days, hepatic organoids were matured and used for subsequent qRT-PCR and BSEP transport analyses. As BSEPspecific substrate, we chose the red-fluorescent Tauro-nor-THCA-24-DBD (Tauro-DBD) substrate, which was added to the medium (HCM, Lonza) of Matrigel-retrieved organoids and incubated for given time points at 37 °C. For LNP transduction of rescuing mRNAs, organoids were incubated for 90 min with the respective LNP in HCM media with 10 μM RHO-Kinase Inhibitor (Tocris) on a thermal shaker (37 °C, 450 rpm) prior to the last differentiation step and further cultivated in undiluted GelTrex in HCM medium for additional 72h with or without GW4064 (Sigma-Aldrich) stimulation prior to the assays.

RNA preparation, reverse transcription, pre-amplification, and PCR analysis

Total RNA was extracted and purified using the AmoyDx FFPE DNA/RNA Kit, (Amoy Diagnostics Co.) according to the manufacturer's instructions. 100 ng of RNA was reverse transcribed using the High-Capacity cDNA Reverse Transcription Kit (Applied Biosystems). After pre-amplification, qPCR was carried out with different TaqMan Gene Expression Assays (Applied Biosystems). Relative quantification of mRNA was performed according to the comparative $2^{-\Delta\Delta CT}$ method with SDHA as an endogenous control (see SI for detailed information).

Structure modeling and molecular dynamics simulations

To analyze the impact of the variant T296I, the ligandbinding domain (LBD) structure of FXR (Q96RI1-1, residues 248-476) was modeled based on the chenodeoxycholic acid (CDCA)- and NCoA2 peptide-bound X-ray crystal structure of the FXR LBD (PDB ID 6HL1) (15), representing the active state of FXR, using SWISS-MODEL (35). To model the inactive state with H12 not interacting with the LBD core, the loop between helix 11 and H12 was remodeled within PyMOL (Schrödinger, LLC). In detail, residues 460 to 466 (460VNDHKFT466) were removed and re-added, pointing away from the LBD core, followed by the α -helix H12.

MD simulations were performed for both the active and inactive states in the presence of the endogenous ligand CDCA and a short peptide sequence from the NCoA2 protein (sequence KENALLRYLLDKD), containing the signature motif LXXLL for binding to an NR (16). The structural models were prepared for molecular dynamics (MD) simulations using the AMBER21 package (36). Overall, four different

systems were prepared: FXR wildtype in the active state (hereafter termed "active WT"), FXR T296I variant in the active state ("active T296I"), FXR wildtype in the inactive state ("inactive WT"), and FXR T296I variant in the inactive state ("inactive T296I"). Postprocessing and analysis of the MD trajectories were performed with CPPTRAJ (37) implemented in AmberTools21 (36). For further details, please see the SI Methods.

Statistical analysis

Significance tests were performed using the Mann-Whitney U test or Student's t test as indicated in the figure captions. The indicated significance levels are n.s. (not significant), *: $p \le 0.05$, **: $p \le 0.01$, ***: $p \le 0.001$, ****: $p \le 0.0001$.

Data availability

All data required is available in this manuscript.

Supporting information—This article contains Supporting information (11, 13, 15, 23, 33, 34, 36-61).

Acknowledgments-Expert technical assistance by Paulina Philippski and Aileen Nötzold is gratefully acknowledged. We are grateful for computational support by the "Zentrum für Informations und Medientechnologie" at the Heinrich-Heine-Universität Düsseldorf. We thank the Gauss Centre for Supercomputing e.V. (www.gauss-centre.eu) for funding the project [project IDs: VSK33; FIC1; FXR] by providing computing time through the John von Neumann Institute for Computing (NIC) on the GCS Supercomputer JUWELS (62) at Jülich Supercomputing Centre (JSC).

Author contributions—A. B. and A. B. data curation; A. B. and A. B. formal analysis; A. B., A. B., J. S., M. S., S. H., M. G., K. G., S. B., M. B., S. F., V. K., and H. G. investigation, A. B. and A. B. methodology; A. B., A. B., J. S., M. S., E. P., T. C., S. H., M. G., K. G., S. B., M. B., S. F., C. D., A. S., U. B., V. K., and H. G. validation; A. B. and A. B. visualization; A. B. and A. B. writing-original draft; A. B., A. B., J. S., M. S., E. P., T. C., S. H., M. G., K. G., S. B., M. B., S. F., C. D., A. S., U. B., V. K., and H. G. writing-review & editing; E. P., T. C., C. D., A. S., U. B., V. K., and H. G. funding acquisition, E. P., T. C., C. D., A. S., U. B., V. K., and H. G. resources, E. P., T. C., C. D., A. S., U. B., V. K., and H. G. supervision; V. K. and H. G. conceptualization; V. K. and H. G. project administration.

Funding and additional information—This study was supported by the BMBF through HiChol (01GM1904A and 01GM2204A to V. K. and C. D.; 01GM1904A and 01GM2204B to H. G.; 01GM1904B and 01GM2204C to U. B., A. S., E. P., T. C.).

Conflict of interest—The authors declare that they do not have any conflicts of interest with the content of this article.

Abbreviations-The abbreviations used are: AF, activation function; BA, bile acids; FXR, farnesoid X receptor; H12, helix 12; LBD, ligand binding domain; MD, Molecular Dynamics; NCoA2, nuclear receptor coactivator 2; NR, nuclear receptor; OCA, obeticholic chenodeoxycholic acid; PFIC, progressive familial



intrahepatic cholestasis; RMSD, root mean square deviation; RXR, retinoic X receptor.

References

- Bull, L. N., and Thompson, R. J. (2018) Progressive familial intrahepatic cholestasis. Clin. Liver Dis. 22, 657–669
- Felzen, A., and Verkade, H. J. (2021) The spectrum of progressive familial intrahepatic cholestasis diseases: update on pathophysiology and emerging treatments. Eur. J. Med. Genet. 64, 104317
- Sinal, C. J., Tohkin, M., Miyata, M., Ward, J. M., Lambert, G., and Gonzalez, F. J. (2000) Targeted disruption of the nuclear receptor FXR/ BAR impairs bile acid and lipid homeostasis. *Cell* 102, 731–744
- Cariello, M., Piccinin, E., Garcia-Irigoyen, O., Sabbà, C., and Moschetta, A. (2018) Nuclear receptor FXR, bile acids and liver damage: introducing the progressive familial intrahepatic cholestasis with FXR mutations. *Biochim. Biophys. Acta* 1864, 1308–1318
- Gomez-Ospina, N., Potter, C. J., Xiao, R., et al. (2016) Mutations in the nuclear bile acid receptor FXR cause progressive familial intrahepatic cholestasis. Nat. Commun. 7, 10713
- Himes, R. W., Mojarrad, M., Eslahi, A., Finegold, M. J., Maroofian, R., and Moore, D. D. (2020) NR1H4 -related progressive familial intrahepatic cholestasis 5. *J. Pediatr. Gastroenterol. Nutr.* 70. https://doi.org/ 10.1097/MPG.0000000000002670
- Mehta, S., Kumar, K., Bhardwaj, R., Malhotra, S., Goyal, N., and Sibal, A. (2022) Progressive familial intrahepatic cholestasis: a study in children from a liver transplant center in India. J. Clin. Exp. Hepatol. 12, 454–460
- 8. Nayagam, J. S., Miquel, R., Thompson, R. J., and Joshi, D. (2024) Genetic cholestasis in children and adults. *J. Hepatol.* 80, 670–672
- Czubkowski, P., Thompson, R. J., Jankowska, I., et al. (2021) Progressive familial intrahepatic cholestasis farnesoid X receptor deficiency due to NR1H4 mutation: a case report. World J. Clin. Cases 9, 3631–3636
- 10. Pfister, E., Dröge, C., Liebe, R., et al. (2022) Extrahepatic manifestations of progressive familial intrahepatic cholestasis syndromes: presentation of a case series and literature review. Liver Int. 42, 1084–1096
- van Mil, S. W. C., Milona, A., Dixon, P. H., et al. (2007) Functional variants of the central bile acid sensor FXR identified in intrahepatic cholestasis of pregnancy. Gastroenterology 133, 507–516
- 12. Hollingsworth, S. A., and Dror, R. O. (2018) Molecular dynamics simulation for all. *Neuron* 99, 1129–1143
- Saen-Oon, S., Lozoya, E., Segarra, V., Guallar, V., and Soliva, R. (2019) Atomistic simulations shed new light on the activation mechanisms of RORγ and classify it as type III nuclear hormone receptor regarding ligand-binding paths. Sci. Rep. 9, 17249
- Chrisman, I. M., Nemetchek, M. D., de Vera, I. M. S., et al. (2018) Defining a conformational ensemble that directs activation of PPARγ. Nat. Commun. 9, 1794
- Merk, D., Sreeramulu, S., Kudlinzki, D., et al. (2019) Molecular tuning of farnesoid X receptor partial agonism. Nat. Commun. 10, 1–14
- Heery, D. M., Kalkhoven, E., Hoare, S., and Parker, M. G. (1997)
 A signature motif in transcriptional co-activators mediates binding to
 nuclear receptors. *Nature* 387, 733–736
- Xu, H. E., Stanley, T. B., Montana, V. G., et al. (2002) Structural basis for antagonist-mediated recruitment of nuclear co-repressors by PPARα. Nature 415, 813–817
- Kumari, A., Mittal, L., Srivastava, M., Pathak, D. P., and Asthana, S. (2021) Conformational characterization of the Co-Activator binding site revealed the mechanism to achieve the bioactive state of FXR. Front. Mol. Biosci. 8, 1–21
- Kumari, A., Mittal, L., Srivastava, M., Pathak, D. P., and Asthana, S. (2023) Deciphering the structural determinants critical in attaining the FXR partial agonism. *J. Phys. Chem. B* 127, 465–485
- Díaz-Holguín, A., Rashidian, A., Pijnenburg, D., et al. (2023) When two become one: conformational changes in FXR/RXR heterodimers bound to steroidal antagonists. ChemMedChem 18. https://doi.org/10.1002/ cmdc.202200556

- 21. Makishima, M., Okamoto, A. Y., Repa, J. J., et al. (1999) Identification of a nuclear receptor for bile acids. Science 284, 1362–1365
- 22. Parks, D. J., Blanchard, S. G., Bledsoe, R. K., et al. (1999) Bile acids: natural ligands for an orphan nuclear receptor. *Science* 284, 1365–1368
- 23. Chothe, P. P., Pemberton, R., and Hariparsad, N. (2021) Function and expression of bile salt export pump in suspension human hepatocytes. *Drug Metab. Dispos* 49, 314–321
- 24. Song, X., Chen, Y., Valanejad, L., *et al.* (2013) Mechanistic insights into isoform-dependent and species-specific regulation of bile salt export pump by farnesoid X receptor. *J. Lipid Res.* 54, 3030–3044
- Ananthanarayanan, M., Balasubramanian, N., Makishima, M., Mangelsdorf, D. J., and Suchy, F. J. (2001) Human bile salt export pump promoter is transactivated by the farnesoid X receptor/bile acid receptor. J. Biol. Chem. 276, 28857–28865
- Marzolini, C., Tirona, R. G., Gervasini, G., et al. (2007) A common polymorphism in the bile acid receptor farnesoid X receptor is associated with decreased hepatic target gene expression. Mol. Endocrinol. 21, 1769–1780
- Mi, L.-Z., Devarakonda, S., Harp, J. M., et al. (2003) Structural basis for bile acid binding and activation of the nuclear receptor FXR. Mol. Cell 11, 1093–1100
- 28. Renaud, J. P., Rochel, N., Ruff, M., et al. (1995) Crystal structure of the RAR-Gamma ligand-binding domain bound to all-trans retinoic acid. *Nature* 378, 681–689
- 29. Kallenberger, B. C., Love, J. D., Chatterjee, V. K. K., and Schwabe, J. W. R. (2003) A dynamic mechanism of nuclear receptor activation and its perturbation in a human disease. *Nat. Struct. Biol.* 10, 136–140
- Nolte, R. T., Wisely, G. B., Westin, S., Cobb, J. E., Lambert, M. H., Kurokawa, R., et al. (1998) Ligand binding and co-activator assembly of the peroxisome proliferator-activated receptor-γ. Nature 395, 137–143
- 31. Wang, H., Chen, J., Hollister, K., Sowers, L. C., and Forman, B. M. (1999) Endogenous bile acids are ligands for the nuclear receptor FXR/BAR. *Mol. Cell* 3, 543–553
- **32.** Heidari, Z., Chrisman, I. M., Nemetchek, M. D., *et al.* (2019) Definition of functionally and structurally distinct repressive states in the nuclear receptor PPARY. *Nat. Commun.* **10**, 5825
- 33. Lee, H.-K., Lee, Y.-K., Park, S.-H., et al. (1998) Structure and expression of the orphan nuclear receptor SHP gene. J. Biol. Chem. 273, 14398–14402
- **34.** Shinozawa, T., Kimura, M., Cai, Y., *et al.* (2021) High-fidelity druginduced liver injury screen using human pluripotent stem cell–derived organoids. *Gastroenterology* **160**, 831–846.e10
- 35. Waterhouse, A., Bertoni, M., Bienert, S., *et al.* (2018) SWISS-MODEL: homology modelling of protein structures and complexes. *Nucleic Acids Res.* 46, W296–W303
- 36. Case, D. A., Aktulga, H. M., Belfon, K., et al. (2021) Amber 2021, Univ California, San Francisco
- **37.** Roe, D. R., and Cheatham, T. E. (2013) PTRAJ and CPPTRAJ: software for processing and analysis of molecular dynamics trajectory data. *J. Chem. Theor. Comput* **9**, 3084–3095
- Pellicciari, R., Fiorucci, S., Camaioni, E., et al. (2002) 6α-ethyl-chenodeoxycholic acid (6-ECDCA), a potent and selective FXR agonist endowed with anticholestatic activity. J Med Chem 45(17), 3569–3572
- 39. Döring, B., Lütteke, T., Geyer, J., and Petzinger, E. (2012) The SLC10 carrier family: transport functions and molecular structure. *Curr Top Membr*, 105–168
- Grebner, C., Lecina, D., Gil, V., et al. (2017) Exploring binding mechanisms in nuclear hormone receptors by Monte Carlo and X-ray-derived motions. Biophys J 112, 1147–1156
- 41. Fischer, A, and Smieško, M (2019) Ligand pathways in nuclear receptors. *J Chem Inf Model* 59, 3100–3109
- Li, W., Fu, J., Cheng, F., et al. (2012) Unbinding pathways of GW4064 from human farnesoid X receptor as revealed by molecular dynamics simulations. J Chem Inf Model 52, 3043–3052
- Waskom, M. (2021) seaborn: statistical data visualization. J Open Source Softw 6, 3021
- Virtanen, P., Gommers, R., Oliphant, T. E., et al. (2020) SciPy 1.0: fundamental algorithms for scientific computing in Python. Nat Methods 17, 261–272



- 45. Zolfaghari, R., Mattie, F. J., Wei, C.-H., Chisholm, D. R., Whiting, A., and Ross, A. C. (2019) CYP26A1 gene promoter is a useful tool for reporting RAR-mediated retinoid activity. Anal Biochem 577, 98-109
- 46. Bas, D. C., Rogers, D. M., and Jensen, J. H. (2008) Very fast prediction and rationalization of pKa values for protein-ligand complexes. Proteins Struct Funct Bioinforma 73, 765-783
- 47. Maier, J. A., Martinez, C., Kasavajhala, K., Wickstrom, L., Hauser, K. E., and Simmerling, C. (2015) ff14SB: improving the accuracy of protein side chain and backbone parameters from ff99SB. J Chem Theory Comput 11, 3696-3713
- 48. Jorgensen, W. L., Chandrasekhar, J., Madura, J. D., Impey, R. W., and Klein, M. L. (1983) Comparison of simple potential functions for simulating liquid water. J Chem Phys 79, 926-935
- 49. Bayly, C. I., Cieplak, P, Cornell, W., and Kollman, P. A. (1993) A wellbehaved electrostatic potential based method using charge restraints for deriving atomic charges: the RESP model. J Phys Chem 97,
- 50. Vanquelef, E., Simon, S., Marquant, G., et al. (2011) R.E.D. Server: a web service for deriving RESP and ESP charges and building force field libraries for new molecules and molecular fragments. Nucleic Acids Res 39, W511-W517
- 51. Dupradeau, F.-Y., Pigache, A., Zaffran, T., et al. (2010) The R.E.D. tools: advances in RESP and ESP charge derivation and force field library building. Phys Chem Chem Phys 12, 7821
- 52. Wang, F., Becker, J.-P., Cieplak, P., and Dupradeau, F-Y. (Published online 2013) R.E.D. Python: Object oriented programming for Amber force fields, Sanford Burn Prebys Med Discov Institute, Univ Picardie - Jules

- 53. Ryckaert, J.-P., Ciccotti, G., and Berendsen, H. J. (1977) Numerical integration of the cartesian equations of motion of a system with constraints: molecular dynamics of n-alkanes. J Comput Phys 23, 327-341
- 54. Darden, T., York, D., and Pedersen, L. (1993) Particle mesh Ewald: an N ·log (N) method for Ewald sums in large systems. J Chem Phys 98, 10089-10092
- 55. Pastor, R. W., Brooks, B. R., and Szabo, A. (1988) An analysis of the accuracy of Langevin and molecular dynamics algorithms. Mol Phys 65, 1409-1419
- 56. Berendsen, H. J. C., Postma, J. P. M., van Gunsteren, W. F., DiNola, A., and Haak, J. R. (1984) Molecular dynamics with coupling to an external bath. J Chem Phys 81, 3684-3690
- 57. Hopkins, C. W., Le Grand, S., Walker, R. C., and Roitberg, A. E. (2015) Long-time-step molecular dynamics through hydrogen mass repartitioning. J Chem Theory Comput 11, 1864-1874
- 58. Grant, B. J., Rodrigues, A. P. C., ElSawy, K. M., McCammon, J. A., and Caves, L. S. D. (2006) Bio3d: an R package for the comparative analysis of protein structures. Bioinformatics 22, 2695–2696
- 59. Grant, B. J., Skjærven, L., and Yao, X. (2020) The Bio3D packages for structural bioinformatics. Protein Sci 30, 20-30
- 60. Skjærven, L., Yao, X.-Q., Scarabelli, G., and Grant, B. J. (2014) Integrating protein structural dynamics and evolutionary analysis with Bio3D. BMC Bioinform 15, 399
- 61. Humphrey, W., Dalke, A, and Schulten, K. (1996) VMD visual molecular dynamics. J Molec Graph 14, 33-38
- 62. Alvarez, D. (2021) JUWELS cluster and booster: exascale pathfinder with modular supercomputing architecture at Juelich supercomputing centre. J. Large Scale Res. Facil. 7, A183

